Initialization and readout of spin chains for quantum information transport

Initialization and readout of spin chains for quantum information transport

Gurneet Kaur and Paola Cappellaro[1]

Department of Nuclear Science and Engineering, Massachusetts Institute of Technology, Cambridge, MA 02139, USA
E-mail: pcappell@mit.edu

Abstract. Linear chains of spins acting as quantum wires are a promising approach for achieving scalable quantum information processors. Nuclear spins in apatite crystals provide an ideal test bed for the experimental study of quantum information transport, as they closely emulate a one-dimensional spin chain, while magnetic resonance techniques can be used to drive the spin chain dynamics and probe the accompanying transport mechanisms. Here we demonstrate initialization and readout capabilities in these spin chains, even in the absence of single-spin addressability. These control schemes enable preparing desired states for quantum information transport and probing their evolution under the transport Hamiltonian. We further optimize the control schemes by a detailed analysis of ^{19}F NMR lineshape.

[1] Author to whom any correspondence should be addressed.

IOP Institute of Physics $\quad$ **Φ** DEUTSCHE PHYSIKALISCHE GESELLSCHAFT

Contents

1. Introduction

Control over small quantum systems and the ability to perform simple quantum algorithms have been demonstrated on a variety of physical systems ranging from trapped ions [1] and electrons [2], to neutral atoms and molecules in optical lattices [3], to superconducting circuits [4] and semiconductor quantum dots [5], to nuclear and electronic spins [6–8]. Although algorithms involving more than one qubit have been executed [9–14], a vital requirement for a quantum computer—*scalability while preserving fidelity*—has not yet been achieved in any physical system. The use of linear chains of spins as quantum wires to couple basic memory units is a promising approach for addressing this issue [15, 16]. These spin chains have the ability to transmit quantum information via the free evolution of the spins under their mutual interaction [17–22]. While advances in fabrication techniques have rendered physical implementation of spin wires possible [23–26], the level of precision available is not yet adequate. Therefore, natural systems such as crystals where the spin position is precisely set by nature are a preferred choice for exploring such applications.

$\quad$ Owing to their unique geometry, nuclear spin systems in apatite crystals have emerged as a rich test bed to probe quasi-one-dimensional (1D) dynamics, including transport and decoherence [27–30]. The apatite crystal wherein ^{19}F (or ^{1}H) nuclei are aligned along one axis emulates a collection of 1D chains. The dynamics of these spin chains has been studied by various nuclear magnetic resonance (NMR) techniques [31–33]. In our previous work [20, 34], we have shown that the natural dipolar interaction among the spins can be manipulated via the available collective control to simulate the Hamiltonian driving quantum transport. The lack of single-spin addressability in these ensemble systems, however, seems to prevent creating and measuring a single-spin excitation as required to study transport. Still, we demonstrated experimentally in fluorapatite (FAp) [27–29] that one can prepare the spin system in an initial state in which polarization is localized at the ends of the spin chain, a state that simulates well the conditions for spin-excitation transport [34].

In this paper, we take a further step toward enabling the experimental study of quantum transport in spin chains: we introduce a technique for reading out the spins at the chain extremities, and we show how to prepare a two-spin encoded state that is able to transfer quantum information. Although initialization and readout are not perfect, they are sufficient to study the transport dynamics under the double quantum (DQ) Hamiltonian [29, 35], as proved by comparing the experimental results with theoretical models. We further validate the addressability of the ends of the chains by probing the evolution of multiple quantum coherences (MQCs) [36], which present well-characterized state-dependent signatures, and by a detailed analysis of ^{19}F lineshape in FAp.

The techniques we introduce achieve critical tasks for the experimental simulation of quantum information transfer and will make it possible to explore errors affecting the transport fidelities as well as control schemes for mitigating them in an experimental setting, where the interactions among spins are not limited to those tractable by solvable models.

2. Transport in mixed-state spin chains

2.1. Spin chain dynamics

Linear chains of spin-1/2 particles have been proposed as quantum wires to transport quantum information between distant nodes of a distributed quantum computing architecture. Transport can occur even in the absence of individual control of the chain spins, as it is mediated by the spin mutual interactions. In the most widely studied model, energy-conserving spin flip-flops (mediated by the isotropic XY Hamiltonian) drive the transport of a single-spin excitation [17–22]. This model has recently been extended to the case where the initial state of the chain cannot be perfectly controlled, and thus it is found in a mixed state rather than in its ground state [34, 37–40].

Spin chains that are in a maximally mixed state are particularly interesting from the point of view of the experimental study of quantum information transfer. This state, corresponding to infinite temperature, can be easily achieved experimentally and has been shown to provide a direct simulation of pure state transport [34]. Additionally, extension to a mixed-state chain enables using the so-called double quantum (DQ) Hamiltonian,

$$\mathcal{H}_{DQ} = \sum_{j < \ell} \frac{b_{j\ell}}{2} \left(\sigma_j^x \sigma_\ell^x - \sigma_j^y \sigma_\ell^y \right), \tag{1}$$

to drive transport, although it does not conserve the number of spin excitations. Here $b_{j\ell}$ is the dipolar coupling constant and σ^x are the Pauli matrices. This Hamiltonian can be easily obtained from the natural dipolar Hamiltonian with only collective control [20, 34] and is related to the isotropic XY Hamiltonian (which instead cannot be generated from the dipolar interaction) via a similarity transformation. The extension to mixed states and to the DQ Hamiltonian opens up the possibility to study experimentally quantum information transport in nuclear spin chains with NMR techniques. Under our experimental conditions (strong external magnetic field, $B_0 = 7$ T, and room temperature), the initial equilibrium state is the Zeeman thermal state,

$$\rho_{th}'(0) \propto \exp\left(-\varepsilon \sigma^z\right) \approx \mathbb{1} - \varepsilon \sigma^z, \tag{2}$$

where $\sigma^z = \sum_j \sigma_j^z$ and $\epsilon = \gamma B_0 / k_B T$. Since the identity does not evolve and does not contribute to the signal, we will focus on the deviation of the density operator from the maximally mixed

state, $\delta\rho \sim \rho - \mathbb{1}$. In the absence of individual spin addressing, transport within a chain can be studied by preparing a polarization excess at one end of the chain, that is, a state where one spin at the chain extremity is polarized while the remaining spins are fully mixed, $\delta\rho \sim \sigma_1^z$. Because of the symmetry between the two chain ends, the state we can prepare experimentally [27, 28], which we call 'end-polarized state', is given by

$$\delta\rho_{\text{end}}(0) = \sigma_1^z + \sigma_N^z. \tag{3}$$

The end-polarized state simulates the dynamics of a single-spin excitation in a pure-state spin chain. This state can transfer a bit of *classical* information by encoding it in the sign of the polarization. This encoding is, however, not enough to transfer quantum information, which requires additional transfer of information about the phase coherence of a state. A two-qubit encoding allows for the transport of a bit of *quantum* information [34, 39]. For transport via the DQ Hamiltonian, this encoding is given by the basis $|0\rangle_L^{\text{dq}} = |00\rangle$ and $|1\rangle_L^{\text{dq}} = |11\rangle$. Here $|0\rangle$ ($|1\rangle$) represents a spin-1/2 $m_z = \frac{1}{2}$ $(-\frac{1}{2})$ eigenstate, whereas $|00\rangle$ and $|11\rangle$ refer to eigenstates of the first and second spins in the chain. The operator basis for transport via mixed states under the DQ Hamiltonian is thus given by

$$\sigma_{xL}^{\text{dq}} = \frac{\sigma_1^x \sigma_2^x - \sigma_1^y \sigma_2^y}{2}, \quad \sigma_{yL}^{\text{dq}} = \frac{\sigma_1^y \sigma_2^x + \sigma_1^x \sigma_2^y}{2},$$

$$\sigma_{zL}^{\text{dq}} = \frac{\sigma_1^z + \sigma_2^z}{2}, \qquad \mathbb{1}_L^{\text{dq}} = \frac{\mathbb{1} + \sigma_1^z \sigma_2^z}{2}. \tag{4}$$

Starting from any of the above initial states, the evolution under the DQ Hamiltonian directly simulates the transport dynamics within a chain.

In the limit of nearest-neighbor (NN) coupling only, the evolution under the DQ Hamiltonian is exactly solvable by invoking a Jordan–Wigner mapping onto a system of free fermions [29, 41, 42]. The resulting dynamics of most of the observables we analyzed in our experiments has been reported in the literature (see, e.g., [29, 34]) and is reviewed in appendix A for completeness. Isolated, linear spin chains with NN couplings is an accurate model for the experiments, given the experimental time scales used [28]. Comparison of the theoretical model with the experimental results thus allows us to validate our initialization and readout methods.

To gather more insights into the states generated by the evolution under the DQ Hamiltonian, we experimentally measured multi-spin correlations via multiple quantum NMR experiments that reveal the coherence order intensities of a state. Transitions between two collective magnetization eigenstates $|m_z^i\rangle$ and $|m_z^j\rangle$ can be classified by their coherence order n, defined as the difference of their eigenvalues, $n = m_z^i - m_z^j$. More generally, for mixed states the presence of a nonzero matrix element $\langle m_z^j | \rho | m_z^i \rangle$ indicates the presence of an n-quantum coherence. While coherences other than ± 1 cannot be detected inductively, MQC NMR techniques allow measurement of multi-spin state dynamics by indirectly encoding their signatures into single-spin terms (see appendix B). The dynamics of quantum coherence intensities can also be calculated analytically in the limit of NN couplings [20, 34, 42]. We review these results in appendix B.

2.2. Preparing and reading out desired spin states

To probe the quantum transport dynamics it is necessary to prepare the spins at the ends of the chain in a perturbed state (such as $\delta\rho_{\text{end}}$), which is then left to evolve under the transport

Hamiltonian. Furthermore, to observe the transport, measurement of the end-chain spins would be desirable. Unfortunately, in a system of dipolarly coupled homonuclear spins (such as FAp) it is not possible to achieve frequency or spatial addressability of individual spins. Still, here we show that we can approximate these preparation and readout steps with the control at hand, combining unitary and incoherent spin manipulation. A key observation is that even in the absence of frequency addressability, the dynamics of the end-chain spins under the internal dipolar Hamiltonian is different from the rest of the spins in the chain. Indeed, the spins at the ends of the chain are coupled to only one NN, whereas spins in the rest of the chain have two neighbors. This fact can be exploited to experimentally prepare the spins at the chain ends in a desired state [27, 28] as well as subsequently read out this state as explained below.

When the initial thermal equilibrium state is rotated to the transverse plane by a $\pi/2$ pulse, we create a state $\delta\rho = \sum_{k=1}^{N} \sigma_k^x$ which evolves under the internal dipolar Hamiltonian. Due to the fewer numbers of couplings with neighboring spins, the spins at the end of the chain have slower dynamics compared to the rest of the chain. Thus, one can select a particular time t_1 such that, whereas the state of the spins at the ends is still mainly σ^x, the rest of the spins have evolved to many-body correlations. A second $\pi/2$ pulse brings the magnetization of the end spins back to the longitudinal axis, while an appropriate phase cycling scheme cancels out other terms in the state [43, 44]. Starting from the thermal initial state $\delta\rho_{\text{th}} = \sum_k \sigma_k^z$, we used the following pulse sequence and appropriate phase cycling scheme to select the ends of the chains,

$$\pi/2|_\alpha \,—\, t_1 \,—\, \pi/2|_{-\alpha}, \tag{P1}$$

with $\alpha = \{-x, y\}$, to average out terms that do not commute with the total magnetization σ^z. As the phase cycling does not cancel zero-quantum coherences, they will be the main source of errors in the initialization scheme (see [27, 28] and section 3.1). For FAp crystals we found that the optimal t_1 time (which we will call 'end-selection time') is given by 30.3 μs [27, 28]. Further details of how we optimized this time are given in section 3.4.

The end-selection scheme forms the basis for a strategy to prepare other states, presented in equation (4), required for quantum information transport. In order to prepare these encoded states experimentally, we use the following scheme. We first prepare the end-polarized state $\delta\rho_{\text{end}}(0) = \sigma_1^z + \sigma_N^z$ and then let the system evolve under the DQ Hamiltonian for a short time, $t_{\text{dq}} = 14.7\mu$s. The initialization sequence is thus

$$\pi/2|_\alpha \,—\, t_1 \,—\, \pi/2|_\beta \,—\, \mathrm{DQ}^\gamma, \tag{P2}$$

where $\mathrm{DQ}^{\gamma=x}$ is propagation under $U_{\text{MQ}}(t_{\text{dq}}) = \mathrm{e}^{-\mathrm{i}\overline{\mathcal{H}}_{\text{DQ}}t_{dq}}$ and $\mathrm{DQ}^{\gamma=y}$ under $U_{\text{MQ}}^\dagger$ (obtained by a $\pi/2$ phase shift of the pulses in the sequence described in section 3). For $[\alpha, \beta, \gamma] = [-x, x, x]$, the state after the sequence (P2) is approximately given by zero- and double-quantum coherences, $\delta\rho_{\text{end}}(t_{\text{dq}}) \approx \sigma_{1,2}^{\text{zq}} + \sigma_{n-1,n}^{\text{zq}} + \sigma_{1,2}^{\text{dq}} + \sigma_{n-1,n}^{\text{dq}}$, where $\sigma_{i,j}^{\text{zq}} = (\sigma_i^x \sigma_j^y - \sigma_i^y \sigma_j^x)$ and $\sigma_{i,j}^{\text{dq}} = (\sigma_i^x \sigma_j^y + \sigma_i^y \sigma_j^x)$. Applying a DQ filter by the four-step phase cycling scheme,

$$[\alpha, \beta, \gamma] = \{[-x, x, x]; [y, -y, x]; [-x, -x, y]; [y, y, y]\},$$

cancels out the zero-quantum terms and selects the DQ terms, which is our desired state: $\delta\rho_y^L \propto \sigma_{1,2}^{\text{dq}} + \sigma_{n-1,n}^{\text{dq}}$. Similarly, a $\pi/4$ collective rotation around z, prior to the DQ filter, is needed to select the $\delta\rho_x^L$ operator.

A combination of unitary and incoherent spin control can also be used to read out the spins at the end of the chain. In inductively measured NMR, the observable is the collective

magnetization of the spin ensemble, σ^z. To simulate the readout of a different observable, the desired state must be prepared prior to acquisition. Thus, similar to state initialization, we want to turn the collective magnetization σ^z into the end-chain state, $\sigma_1^z + \sigma_N^z$. We call this the 'end-readout step'. We note that the sequence used for readout cannot in general be a simple inversion of the end-selection step (which is not a unitary, reversible operation). Proper phase cycling should ensure that the state prior to the end-selection sequence has contributions mainly from population terms ($\propto \sigma_k^z$). For example, two-step phase cycling [43] is enough to select populations and zero-quantum terms, which in turn can be eliminated by purging pulses [45]. In general, an efficient phase cycling scheme of the overall sequence can be selected by the coherence transfer pathway method [44] based on the evolved state. Since the states produced from evolution under the DQ Hamiltonian in 1D systems are already of the form $\propto \sigma_k^z + \sigma_{k,h}^{\text{dq}}$, the sequence (P1) with a two-step phase cycling is enough for the end-readout step.

3. Experimental methods

Experiments were performed in a 7 T wide-bore magnet with a 300 MHz Bruker Avance spectrometer and a probe tuned to 282.4 MHz for ^{19}F measurement. A pure, single crystal of fluorapatite [$Ca_5(PO_4)_3F$] grown by the flux method was used for the measurements [46]. The long relaxation time ($T_1 = 1100$ s) of ^{19}F spins indicates a low concentration of paramagnetic impurities, but other defects interrupting the chains, such as vacancies, are expected to be present. FAp crystals have a hexagonal geometry with space group P63/m. The ^{19}F nuclei form linear chains along the c-axis, each surrounded by six other chains. The intra-nuclear spacing within a single chain is $d = 0.3442$ nm and chains are separated by $D = 0.9367$ nm. When placed in a strong magnetic field, the nuclear spins interact via the secular dipolar Hamiltonian,

$$\mathcal{H}_{\text{dip}} = \sum_{j<\ell}^n b_{j\ell} \left[\sigma_j^z \sigma_\ell^z - \frac{1}{2} \left(\sigma_j^x \sigma_\ell^x + \sigma_j^y \sigma_\ell^y \right) \right], \tag{5}$$

where the couplings depend on the relative positions $\vec{r}_{j\ell}$ as $b_{j\ell} = (\mu_0/16\pi)(\gamma^2 \hbar / r_{j\ell}^3)(1 - 3\cos^2\theta_{j\ell})$, with μ_0 the standard magnetic constant, γ the gyromagnetic ratio, $r_{j\ell}$ the distance between nucleus j and ℓ, and $\theta_{j\ell}$ the angle between $\vec{r}_{j\ell}$ and the z-axis. Due to $1/r^3$ dependence of dipolar coupling, the largest ratio of in-chain to cross-chain coupling is close to 40. For our experiments, the crystal was aligned parallel to the external magnetic field in order to maximize this ratio. It has been shown that under these settings and for short evolution times, couplings across different chains can be neglected and the system can be considered as a collection of 1D chains [28].

We performed two sets of experiments for each of the different initial states and readouts. First we probed the transport dynamics driven by the DQ Hamiltonian. For this purpose, the collective or end-chain magnetization was measured as we increased the evolution time t under the DQ Hamiltonian. We used a standard eight-pulse sequence [47] to implement the DQ Hamiltonian. The length of the $\pi/2$ pulse was 1.45 μs. The evolution time was incremented by varying the inter-pulse delay from 1 to 6.2 μs and the number of loops was increased from 1 to 12 (varying both the parameters enabled exploring a wider range of evolution times). A recycle delay of 3000 s was used for these measurements. We restricted the evolution to a time scale where the ideal model applies, and errors arising from leakage to other chains and next-NN

couplings are small [28]. In this time scale, the initial perturbation travels across ≈17 spins [29] and only the polarization starting from one end of the chain and moving away toward the other end was observed; observing the polarization reach the other end is further complicated by the distribution of chain lengths. However, since the dynamics of chains under the DQ Hamiltonian shows appreciable differences between the thermal and the end-polarized state, experimental verification of initial state preparation is possible even at these short time scales.

In the second set of experiments, we let the initial state evolve under the DQ Hamiltonian and measured the MQCs to gather more information on the evolved state (see appendix B for details of the experimental method). The inter-pulse delay was varied from 1 to 6 μs and the number of loops was increased from 1 to 3. We encoded coherences up to order 4 with a $K = 4$ step phase cycling. Since these measurements involve phase cycling, a shorter recycle delay of 1000 s could be used.

### 3.1. Experimental results: spin transport

Figure 1(a) shows the observed evolution of the collective magnetization σ^z under the DQ Hamiltonian, starting from the thermal initial state, $S^{\mathrm{th}}(t) \propto \mathrm{Tr}\{U_{\mathrm{MQ}}\delta\rho_{\mathrm{th}}U_{\mathrm{MQ}}^{\dagger}\sigma^z\}$, with $U_{\mathrm{MQ}}(t) = \mathrm{e}^{-\mathrm{i}\overline{\mathcal{H}}_{\mathrm{DQ}}(t)}$. The data points were fitted with the analytical function (equation (A.1)) described in appendix A. In figure 1(b), we plot the system dynamics starting from an end-polarized state, equation (3) (where polarization is localized at the ends of the chain), and reading out the collective magnetization, $S^{\mathrm{se}}(t) \propto \mathrm{Tr}\{U_{\mathrm{MQ}}\delta\rho_{\mathrm{end}}U_{\mathrm{MQ}}^{\dagger}\sigma^z\}$. Figure 1(c) shows a complementary measurement where we start from the thermal initial state, given by the collective magnetization, and read out the ends of the chains after evolution under the DQ Hamiltonian, $S^{\mathrm{re}}(t) \propto \mathrm{Tr}\{U_{\mathrm{MQ}}\delta\rho_{\mathrm{th}}U_{\mathrm{MQ}}^{\dagger}\delta\rho_{\mathrm{end}}\}$. Both these data sets were fitted by the analytical expression (A.2). As is evident from near-perfect fitting, the analytical model explains the experimental data quite precisely.

Figures 1(a) and (b) show very different chain dynamics for the two initial states (with and without end selection), giving an experimental validation of our initialization method. Furthermore, the data and fittings for end selection (figure 1(b)) and end readout measurements (figure 1(c)) are very similar. This indicates the robustness of the readout step. Finally, figure 1(d) shows the evolution of the end-polarized initial state under the DQ Hamiltonian, measured using the 'end-readout step' (P2), $S^{\mathrm{sre}}(t) \propto \mathrm{Tr}\{U_{\mathrm{MQ}}\delta\rho_{\mathrm{end}}U_{\mathrm{MQ}}^{\dagger}\delta\rho_{\mathrm{end}}\}$. The fitting function used is given in equation (A.3), which has the same form as the transport of a single excitation in a pure state chain [19, 34]: this experiment is thus a direct simulation of spin transport.

In all the above fittings, we used the following fitting parameters: a scalar multiplier, a baseline constant, the NN dipolar coupling and a shift of the time axis. The shift of the time axis is needed since there is a delay of a few μs between the end of the multiple pulse sequence (ideally $t = 0$) and the measurement of the signal. From the fit we obtain a value for the dipolar coupling of 8.161, 8.172, 8.048 and 8.63 × 10³ rad s⁻¹ for the four experiments, respectively. Except for the last experiment, the other values agree well with those obtained from similar measurements made on a different FAp crystal [28] and also with the theoretical value $b = 8.17 \times 10^3$ rad s⁻¹ resulting from the known structure of FAp.

The small discrepancy in the fitting parameter for the last experiment, where we are initializing and reading out the chain ends, can be explained by imperfections of the end-select and readout schemes. Unfortunately, the phase cycling scheme does not cancel out zero-quantum terms. Thus, residual polarization on spins 2 and $N-1$ as well as correlated states
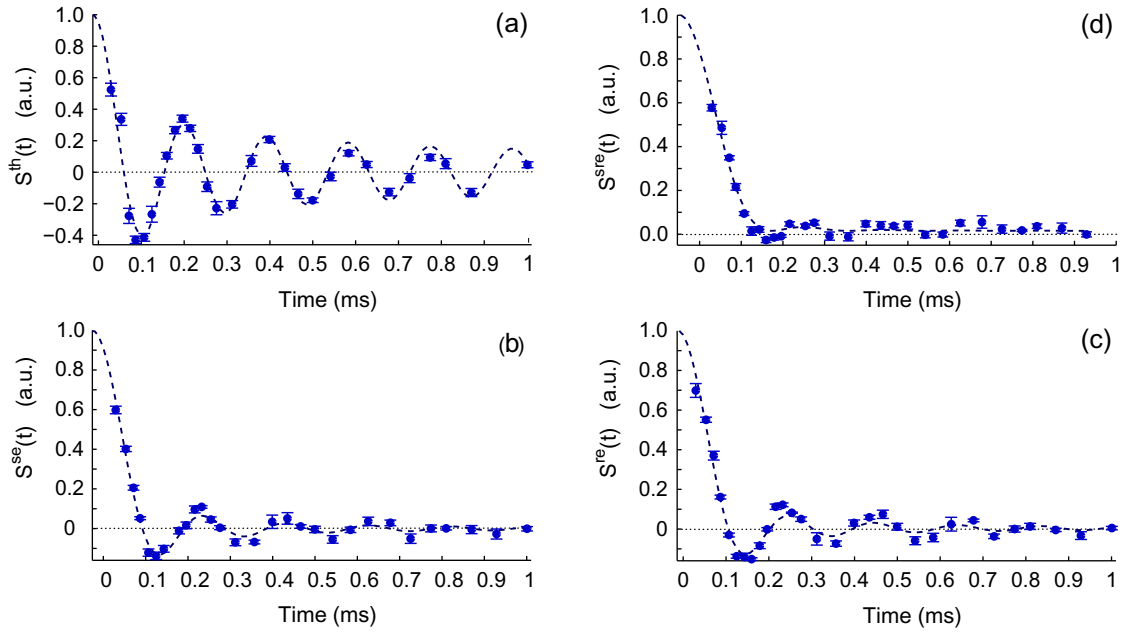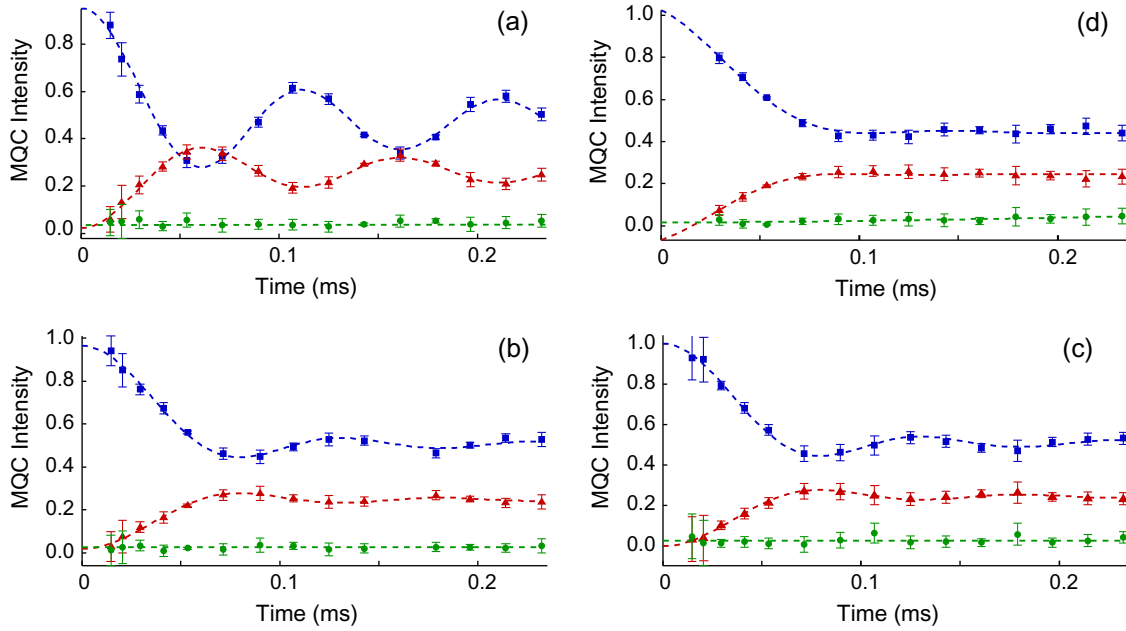
Figure 1. Evolution under the DQ Hamiltonian: (a) Initial state: $\delta\rho_{\text{th}}$. Readout: collective magnetization, σ^z. (b) Initial state: $\delta\rho_{\text{end}}$. Readout: collective magnetization. (c) Initial state: $\delta\rho_{\text{th}}$. Readout: end readout. (d) Initial state: $\delta\rho_{\text{end}}$. Readout: end readout. Circles are the experimental data (collective magnetization in (a) and (b) and end of chain magnetization in (c) and (d)). The measurement was carried out using a single scan in (a), two scans in (b) and (c) for two-step phase cycling and four scans in (d) for four-step phase cycling. The lines are the fits using the analytical model described in appendix A. Error bars are given by the offset of the signal from zero. The fitting gives the following values for the dipolar coupling: 8.165 (a), 8.172 (b), 8.048 (c) and 8.63 (d) $\times 10^3$ rad s^{-1}.

of the form $\sigma_j^z(\sigma_{j-1}^+\sigma_{j+1}^- + \sigma_{j-1}^-\sigma_{j+1}^+)$ contribute to errors, lowering the fidelity with the desired state. This effect is more important for the last experiment, since errors in the two selection steps accumulate. Moreover, the end readout scheme works well only if applied to the ideal state that is expected after transport. The deviation of the prepared initial state from the ideal state further contributes to the error in the final measured data. Still, the agreement of the experimental data with the analytical model indicates that these errors are small and do not invalidate the scheme.

3.2. Experimental results: multiple quantum coherences

We present the results of the second set of experiments in figure 2, which shows the evolution of the zero-, second- and fourth-order coherence intensities $I'_n(t)$, experimentally measured for different initial states and readouts according to equation (B.2). Figure 2(a) shows the usual MQC signal, obtained measuring the collective magnetization and starting from an initial thermal state (equation (2)). The data points are fitted by functions (B.3) in appendix B. The only parameter used in these fittings was the dipolar coupling constant, for which we obtained the value $b = 7.971 \times 10^3$ rad s^{-1}. The data shown in figure 2(b) have been measured by first

Figure 2. Evolution of MQCs $I'_n(t)$ (0Q blue squares, 2Q red triangles, 4Q green circles): (a) Initial state: $\delta\rho_{th}$. Readout: collective magnetization. (b) Initial state: $\delta\rho_{end}$. Readout: collective magnetization. (c) Initial state: $\delta\rho_{th}$ Readout: end-readout. (d) Initial state: $\delta\rho_{end}$. Readout: end-readout. Circles are the experimental data (collective magnetization in (a) and (b) and end of chain magnetization in (c) and (d)). The measurement was carried out using a single scan in (a), two scans in (b) and (c) for two-step phase cycling and four scans in (d) for four-step phase cycling. The data points are fitted by analytical functions (blue and red lines) obtained from the DQ Hamiltonian with NN couplings (equations (B.3)–(B.5)) for panels (a)–(d), respectively. The 4Q coherences (which should be zero in the ideal model) were simply fitted with a constant. The error bars are estimated from the deviation of first-order quantum coherence from zero. Fitting of the data gives dipolar coupling: 7.971 (a), 8.077 (b), 8.031 (c) and 8.492 (d) $\times 10^3$ rad s^{-1}.

selecting the ends of the chain and then carrying out the MQC measurement where collective magnetization is read out. Figure 2(c), on the other hand, shows the data for MQC measurements starting from the thermal initial state but reading out only the spins at the chain ends. Both these data were fitted by the analytical functions (B.4), giving $b = 8.077$ and 8.031×10^3 rad s^{-1}, respectively. This is in very good agreement with the values obtained from the quantum transport measurements. We remark again that the results obtained from end-selection, figure 2(b), and end-readout measurements, figure 2(c), are very similar, thus validating the effectiveness of the readout step. The data for the case where we initialize the ends of the chains before letting the system evolve under the DQ Hamiltonian and then read out the ends are shown in figure 2(d). Good fitting of the data with equation (B.5) was obtained for $b = 8.492 \times 10^3$ rad s^{-1} and shifting the time axis by $15\,\mu$s. As mentioned earlier, we expect the errors in selecting the ends of the chains to add up in the experimental data, resulting in a slightly higher value of the fitting parameter b. The first two data points in the above-mentioned figures were measured
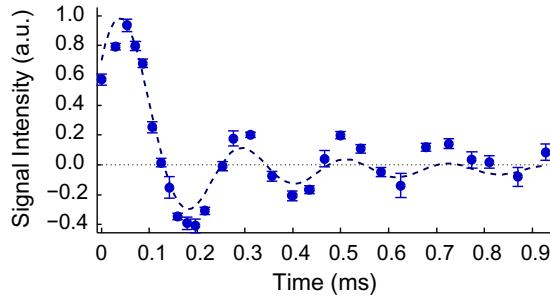
Figure 3. Experimental dynamics of the logical state $\delta\rho_y^L$ (equation (4)). The logical initial state was prepared as described in section 2.2 and its evolution under the DQ Hamiltonian was monitored by observing the collective magnetization. Dots are the experimental data and lines are the fits using the analytical model described in appendix A (equation (A.4)). The fitting of the data points gives a dipolar coupling value of $7.551 \times 10^3 \, \mathrm{rad \, s^{-1}}$.

using a four-pulse sequence to implement the DQ Hamiltonian (instead of a standard eight-pulse sequence), leading to greater error bars for these data points.

3.3. Quantum information transport

To demonstrate our ability to experimentally simulate not only the transport of *classical* information, as encoded in the spin polarization, but also of *quantum* information, we prepared and studied the evolution of one of the logical states in equation (4). The logical state $\delta\rho_y^L$ was prepared by the scheme described in section 2.2 (similar schemes could be used to prepare the other states in the operator basis). Figure 3 shows the evolution of this state under the DQ Hamiltonian that simulates experimentally the transport of quantum information via a maximally mixed quantum channel. The dynamics was monitored by measuring the collective magnetization, $S^L \propto \mathrm{Tr}\{U_{MQ}\delta\rho_y^L U_{MQ}^{\dagger}\sigma^z\}$. The data points were fitted by the expression in equation (A.4) giving the value of the dipolar coupling constant as $7.551 \times 10^3 \, \mathrm{rad \, s^{-1}}$. We note that the scheme for preparing this logical state involves selecting the ends of the chain and then creating MQC and filtering out all the terms except the DQ terms. The errors involved in both these steps add up and result in deviation of the measured data points from the analytical function. The experimental results, however, follow the expected analytical model and the dipolar coupling constants obtained from these experiments agree very well with those obtained from other measurements.

In all of the above-described measurements, where the ends of the chains were selected and initialized, we used $t_1 = 30.3 \, \mu$s in the pulse sequence (P1). As described above, this value was obtained by selecting the time when polarization of the spins at the ends of the chains is nonzero while it has decayed to zero for the other spins, as a result of evolution under the internal dipolar Hamiltonian. In order to confirm this value experimentally, we repeated the transport and MQC measurements at different values of t_1 (not shown here). We observed that $t_1 = 30.3 \, \mu$s gave the best fittings with the analytical functions, pointing toward the fact that the fidelity of end selection is highest for $t_1 = 30.3 \, \mu$s. This is further confirmed by a detailed ^{19}F NMR lineshape analysis as described in the next section.
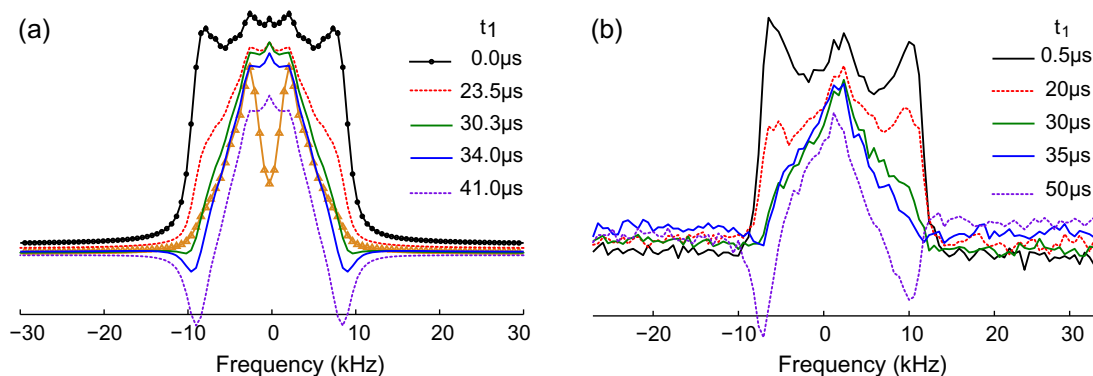
Figure 4. (a) Simulated ^{19}F lineshapes for a chain of 11 spins, for the thermal initial state (circles), the ideal end-polarized state (triangles) and for an initial state prepared via a simulated P1 sequence, with varying t_1 times. (b) Experimentally measured ^{19}F NMR lineshape after state initialization performed with the sequence (P1) for various t_1 times. Solid lines are for $t_1 = 30$ and $35\,\mu$s, which give the narrowest linewidth and the best state preparation.

3.4. ^{19}F nuclear magnetic resonance lineshape analysis

A system comprising linear chains of spins, such as FAp, is of immense interest for NMR lineshape calculations by virtue of the simplicity it offers as compared to a 3D system [48, 49]. The ^{19}F spins in FAp have a characteristic three-peak lineshape, which shows strong angular dependence [50]. In our study, we utilize this angular dependence to align the crystal parallel to the external magnetic field in order to minimize inter-chain couplings.

The lineshape provides signatures not only of the system dimensionality, but also of its initial state; thus we expect to see qualitative differences in the NMR spectra for the thermal and end polarized states. We calculated the free induction decay (FID) for a chain of $N = 11$ ^{19}F nuclear spins evolving under the secular dipolar Hamiltonian (equation (5)) with coupling $b = 8.1 \times 10^3\,\text{rad s}^{-1}$. These calculations were also performed for the end-polarized state, obtained by simulating the sequence (P1) for different values of the end-selection time (t_1). The NMR spectra obtained from these simulations are shown in figure 4(a), together with the lineshapes for the thermal state (equation (2)) and the ideal end-polarized state (equation (3)). A few observations are worth mentioning. The NMR linewidth shows a progressive narrowing as t_1 is increased starting from $t_1 = 0\,\mu$s (corresponding to the thermal state). The linewidth is narrowest for $t_1 = 30.3\,\mu$s and then starts increasing gradually, but now with an anti-phase (dispersive) component. A simple explanation of these features can be obtained by considering the signal as arising from a competition between the signal of the end-chain spins and the signal of the spins in the bulk. The spins at the chain extremities are dipolarly coupled to only one spin; hence, we expect a splitting of the NMR line into a doublet. The spins in the chain, instead, are each coupled to two NNs and hence produce a broader NMR line, split into a triplet. As the first contribution increases with increasing t_1 time, the linewidth narrows. At even longer times (t_1 beyond 30.3 μs), two-spin correlations are created that give rise to a dispersive spectrum under subsequent dipolar Hamiltonian evolution. These anti-phase terms keep increasing for longer t_1 times. We observe that none of the simulated lines exactly replicates the expected lineshape for the ideal end-polarized state. This is due to the less than 100%
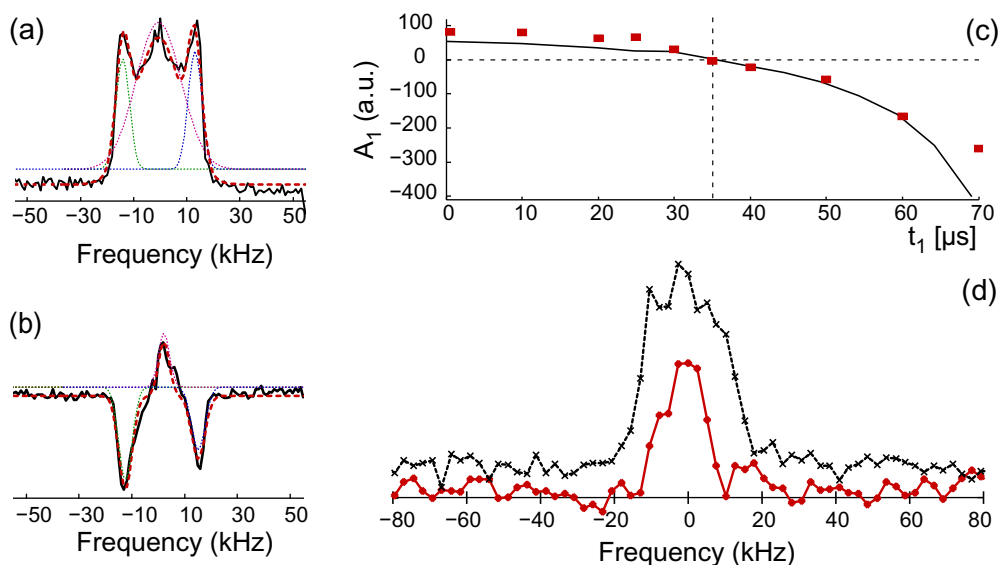
Figure 5. (a) The ^{19}F NMR lineshape (for $t_1 \mu$s) can be fitted by three Gaussian lines. Individual Gaussian lines are shown as thin dotted lines; the sum of the lines is thick red. (b) The ^{19}F NMR lineshape (for $t_1 = 60 \mu$s) can be fitted by three Gaussian lines out of which two lines have negative amplitude. (c) Amplitude A_1 of the first Gaussian line as a function of t_1 used to fit the experimental data (red squares) and simulated spectra (black line). (d) ^{19}F NMR lineshape measured for thermal (black, dotted) and end-polarized (red) initial states using the pulse sequence P3.

fidelity of end-selection and initialization steps, as explained in section 3.1. The simulated lineshapes are, however, in good agreement with the corresponding experimentally measured lineshapes (figure 4(b)), apart from a slight asymmetry, which might have been introduced by a misalignment of the crystal with respect to the magnetic field. In particular, the experimental spectra for $t_1 = 30$ and 35μs have a width very close to the ideal end-selected spectrum.

In order to draw a quantitative comparison between simulated and measured NMR spectra, we fit the lineshapes at different t_1 times with a model comprising three Gaussian lines, at frequencies shifted by the NN dipolar coupling. As shown in figure 5, both simulated and experimental lineshapes could be fitted reasonably well with this model. Since the outer lines in the Gaussian model arise only from the spins inside the chains, their amplitude is expected to show a zero crossing at t_1 where the chain extremities have the maximum contribution to the measured lineshape and the bulk spin polarization has a very small contribution. In our data, this is seen at 35μs, indicating that end selection has maximum fidelity for this value of t_1. This is in close agreement with the 30.3μs obtained from an optimization of the DQ-Hamiltonian evolution fitting and used in our measurements.

In the lineshape analysis described above, all the NMR measurements were carried out by using a $\pi/2$ pulse and measuring the resultant FID. This scheme reads out the collective magnetization from all the nuclei within the chains. It would be interesting to isolate the signal contribution from the nuclei located at the chain ends. This was achieved by means of the pulse

sequence (P3),

$$\text{P1}—\pi/2—(\tau)—\pi/2—\text{P1}, \tag{P3}$$

where the end-selection step (sequence (P1)) is used to polarize as well as to read out the nuclei at the chain ends. The selection and readout steps are separated by a variable delay (τ) that enables measurement of FID (evolution under the natural dipolar Hamiltonian) as a function of time. Fourier transform of this FID results in an NMR lineshape where only the nuclei at the chain ends contribute.

The measured lineshapes for thermal initial ($t_1 = 0\,\mu$s) and end-polarized ($t_1 = 30.3\,\mu$s) states using the sequence (P3) are shown in figure 5(d). Due to the long T_1 of ^{19}F nuclei, it was not possible to measure as many points as in standard FID measurements. This resulted in a low resolution of the Fourier transformed signal, and hence the three characteristic peaks of FAp lineshape are not properly resolved. Nonetheless, differences in the lineshape and line width between the two signals are clearly visible.

4. Conclusion

In conclusion, we have studied spin initialization and readout techniques in linear chains of nuclear spins and experimentally demonstrated partial addressability of spins at the ends of the chain by means of NMR control schemes. We have shown that even though NMR implementation allows only collective control and observables, we could achieve initialization as well as readout capabilities through a combination of coherent and incoherent control. These techniques can be used to prepare the state of relevance for quantum information transport as well as to monitor the dynamics of the end-chain spins as it evolves under the DQ Hamiltonian obtained via collective manipulation of the natural dipolar interaction. We validated our method by comparing the experimental results with analytical solutions based on an idealized model, which applies to the time scales explored in the experiment. The good agreement of the data with the analytical formula confirms the preparation and readout of the desired state.

In addition, we probed the states and their evolution by means of MQC measurements, which reveal information about multi-spin correlations. Again, good conformity of the experimental results with the theoretical model was observed. We further optimized the end-selection scheme by a detailed analysis of the F^{19} NMR lineshapes obtained from collective thermal magnetization and the end-polarized state, respectively.

Although we cannot achieve universal control of the end-chain spins and do not detect the polarization reaching the end of the chain, the initialization and readout capabilities demonstrated in this work will allow us to experimentally characterize quantum transport in spin chains. It will enable us, for example, to explore non-idealities that emerge, e.g., at longer times from non-NN couplings as well as couplings to other chains, and from the interaction of the chains with the environment. Additionally, these methods will allow further experimental studies of control schemes that can enable perfect fidelity transfer.

crystal used in this work. We thank Lorenza Viola and Chandrasekhar Ramanathan for fruitful discussions.

Appendix A. Analytical solution for the evolution under the double quantum Hamiltonian

Information transport in linear spin chains has often been studied in the literature as arising from the evolution under the isotropic XY Hamiltonian, $\mathcal{H}_{XY} = \sum_{j<\ell} \frac{b_{j\ell}}{2}(\sigma_j^x \sigma_\ell^x + \sigma_j^y \sigma_\ell^y)$. For mixed-state chains, we showed that the DQ Hamiltonian (equation (1)) can as well drive the transport, since it is connected to the XY Hamiltonian by a similarity transformation. We can thus simulate quantum transport with a Hamiltonian that (unlike the XY Hamiltonian) can be implemented experimentally using dipolar Hamiltonian and collective radio-frequency (RF) pulses using a standard sequence [36, 47].

The evolution of the 1D spin system under a DQ Hamiltonian is exactly solvable in the NN limit (only NN couplings are present and all are equal to b), by invoking a Jordan–Wigner mapping onto a system of free fermions [27, 36, 42, 47]. Various formulae describing different initial states and observables have been reported [20, 29, 34], and we reproduce here the formulae we used to interpret our experimental results in the main text.

The analytical solutions for the evolution of the thermal state and end-polarized state, when measuring the collective magnetization, are given by

$$S^{\text{th}}(t) = \sum_{p=1}^{N} A_{p,p}(2t), \tag{A.1}$$

$$S^{\text{se}}(t) = \sum_{p=1}^{N} A_{1,p}^2(t), \tag{A.2}$$

with

$$A_{j,q}(t) = \sum_{m=0}^{\infty} i^{2m\nu}[i^\delta J_{2m\nu+\delta}(2bt) - i^\sigma J_{2m\nu+\sigma}(2bt)] + \sum_{m=1}^{\infty} i^{2m\nu}[i^{-\delta} J_{2m\nu-\delta}(2bt) - i^{-\sigma} J_{2m\nu-\sigma}(2bt)],$$

where $\nu = N+1$, $\delta = q - j$, $\sigma = q + j$ and J_n are the nth order Bessel functions of the first kind. $S^{\text{th}}(t)$ is the collective magnetization measured after DQ evolution starting from the thermal initial state and $S^{\text{se}}(t)$ is the collective magnetization measured after DQ evolution starting from the end-polarized initial state. We note that the collective magnetization (thermal state) evolution would give the same signal when one measures the end-polarized state, so that $S^{\text{se}}(t) = S^{\text{re}}(t) \equiv S^{\text{end}}(t)$.

Transport from one end of the chain to the other is described by

$$S^{\text{sre}}(t) = A_{1,1}^2(t) + A_{1,N}^2(t), \tag{A.3}$$

which corresponds to the experimental situation where we prepared the end-polarized state and measured the chain ends only. Finally, we can derive the expected signal arising from the collective magnetization when the initial state is the logical state $\delta\rho_{yL}$:

$$S^{\text{yL}}(t) = A_{1,2}(2t) + A_{N-1,N}(2t). \tag{A.4}$$

Appendix B. Multiple quantum nuclear magnetic resonance spectroscopy

Multiple quantum spectroscopy is a powerful technique in NMR. It has the ability to simplify complex spectra by revealing some of the forbidden transitions. Additionally, the creation and evolution of quantum coherences can be used to probe the dynamics of a correlated many-spin system giving insight into dimensionality of the spin system, distribution of coupling constants and effects of motions and quantum transport [36, 51–56].

A density matrix describing the spin system may be expressed as $\rho(t) = \sum_n \rho_n(t)$, where $\rho_n(t)$ is the contribution to $\rho(t)$ from MQC of order n. The intensities of MQC are given by $I_n(t) = \text{Tr}[\rho_n(t)\rho_{-n}(t)]$ and can be obtained by performing the experimental scheme described below.

MQC are first excited by driving the spin system by irradiation with cycles of multiple pulse sequences consisting of RF pulses and delays. For example, the so-called DQ Hamiltonian (equation (1)) creates even quantum coherences from the longitudinal magnetization. This Hamiltonian can be created using a standard eight-pulse sequence [47] or a symmetrized 16-pulse sequence [36]: The primitive pulse cycle is given by P4 $= \frac{\delta t}{2} - \frac{\pi}{2}|_x - \delta t' - \frac{\pi}{2}|_x - \frac{\delta t}{2}$, where $\delta t' = 2\delta t + w$, δt is the delay between pulses and w is the width of the $\pi/2$ pulse. To first-order average Hamiltonian, this sequence simulates the DQ Hamiltonian, while the eight-pulse sequence, P8 $= $P4 $\cdot \overline{\text{P4}} \cdot \overline{\text{P4}} \cdot$ P4, where $\overline{\text{P4}}$ is the time-reversed version of P4, gives $\overline{\mathcal{H}}_{\text{DQ}}$ to second order and the 16-pulse sequence, P8 $\cdot \overline{\text{P8}}$, compensates for pulse errors.

Since standard NMR techniques measure only single-quantum coherences, in order to probe the MQC dynamics it is necessary to indirectly encode their signature into single-quantum coherences, which can be directly measured inductively. This is done by labeling each coherence order with a different phase If ρ_i is the initial density matrix, the final density matrix ρ_f is given by

$$\rho_f = U_{\text{MQ}}^\dagger U_\phi U_{\text{MQ}} \rho_i U_{\text{MQ}}^\dagger U_\phi^\dagger U_{\text{MQ}},$$

where $U_{\text{MQ}} = \exp(-i\overline{\mathcal{H}}_{\text{DQ}}t)$, and $U_\phi = \exp(-i\phi\sigma_z/2)$ is a rotation about the z-axis by an angle ϕ. Under this rotation, a coherence term of order n will acquire a phase $n\phi$. The readout is performed by using an appropriate sequence in order to measure ρ_i. In order to extract the information about the distribution of MQC, each measurement must be repeated while incrementing ϕ from 0 to 2π in steps of $\delta\phi = 2\pi/2K$, where K is the highest order of MQC we wish to encode. Finally, Fourier transform of the signal with respect to ϕ yields the coherence order intensity:

$$I_n(t) = \sum_{k=1}^K S_i^k(t)\, e^{-ikn\delta\phi}, \tag{B.1}$$

where $S_i^k(t) = \text{Tr}\{\rho_f^k(t)\rho_i\}$ is the signal acquired in the kth measurement. Often it is not possible or convenient to measure ρ_i and only another observable ρ_{obs} is accessible (e.g. a $\pi/2$ pulse can be used to read out the collective magnetization σ_z at the end of the experiment). In this case, starting from an initial state ρ_i, the signal $S_{\text{obs}}^k = \text{Tr}\{\rho_f^k(t)\rho_{\text{obs}}\}$ yields the coherence order intensity

$$I_n'(t) = \sum_{k=1}^K S_{\text{obs}}^k(t)\, e^{-ikn\delta\phi} = \text{Tr}\{\rho_i(t)^n \rho_{\text{obs}}(t)^{-n} + \rho_i(t)^{-n}\rho_{\text{obs}}(t)^n\}, \tag{B.2}$$

where $\rho_i(t) = U_{\text{MQ}}\rho_i U_{\text{MQ}}^\dagger$ and $\rho_{\text{obs}}(t) = U_{\text{MQ}}\rho_{\text{obs}} U_{\text{MQ}}^\dagger$.

The technique of MQC spectroscopy outlined above is particularly well suited to study information transport by means of the DQ Hamiltonian, since the coherence intensities show characteristic signatures of the occurred transport [20].

In a 1D system with NN coupling, only zero- and double-quantum coherence orders are created by the DQ Hamiltonian [42]. Starting from the thermal initial state, the normalized intensities (as defined in equation (B.1)) of the zero- and double-quantum coherences predicted by the analytical model are given by (see equation (61) of [52]):

$$J_0^{\text{th}}(t) = \frac{1}{N} \sum_k \cos^2[4bt \cos(\psi_k)],$$

$$J_2^{\text{th}}(t) = \frac{1}{2N} \sum_k \sin^2[4bt \cos(\psi_k)],$$

(B.3)

where, as before, N is the number of spins in the chain and $\psi_k = k\pi/(N+1)$.

For the end-select state, zero- and double-quantum coherence intensities (as defined in equation (B.2)) are given by the analytical model as follows:

$$J_0^{\text{end}}(t) = \frac{2}{N+1} \sum_k \sin^2(\psi_k) \cos^2[4bt \cos(\psi_k)],$$

$$J_2^{\text{end}}(t) = \frac{1}{N+1} \sum_k \sin^2(\psi_k) \sin^2[4bt \cos(\psi_k)].$$

(B.4)

In both equations (B.3) and (B.4), the normalization is chosen such that $J_0 + 2J_2 = 1$.

In the case when the chain end selection is operated for both initialization and readout, the MQC signal corresponds to equation (B.1) and the normalized zero and DQ intensities are given by [20]

$$J_0^{\text{sre}}(t) = \frac{4}{(N+1)^2} \sum_{k,h} \sin^2(k) \sin^2(h) \cos^2(\psi_k + \psi_h)(1 + \cos[Nk+k]\cos[Nh+h]),$$

$$J_2^{\text{sre}}(t) = \frac{2}{(N+1)^2} \sum_{k,h} \sin^2(k) \sin^2(h) \sin^2(\psi_k + \psi_h)(1 + \cos[Nk+k]\cos[Nh+h]),$$

(B.5)

where the superscript 'sre' refers to select and read ends.

Finally, for the logical state $\delta\rho_{y\text{L}}$, the MQC intensities are as follows:

$$J_0^{y\text{L}}(t) = \frac{2}{N+1} \sum_{k=1}^{N} \sin(\psi_k) \sin(2\psi_k) \sin(8bt \cos \psi_k),$$

$$J_2^{y\text{L}}(t) = \frac{-1}{N+1} \sum_{k=1}^{N} \sin(\psi_k) \sin(2\psi_k) \sin(8bt \cos \psi_k).$$

(B.6)

References

[1] Cirac J I and Zoller P 1995 Quantum computations with cold trapped ions *Phys. Rev. Lett.* **74** 4091–4
[2] Ciaramicoli G, Marzoli I and Tombesi P 2003 Scalable quantum processor with trapped electrons *Phys. Rev. Lett.* **91** 017901

[3] Monroe C 2002 Quantum information processing with atoms and photons *Nature* **416** 238–46

[4] Vion D, Aassime A, Cottet A, Joyez P, Pothier H, Urbina C, Esteve D and Devorett M H 2002 Manipulating the quantum state of an electrical circuit *Science* **296** 886

[5] Petta J R, Johnson A C, Taylor J M, Laird E A, Yacoby A, Lukin M D, Marcus C M, Hanson M P and Gossard A C 2005 Coherent manipulation of coupled electron spins in semiconductor quantum dots *Science* **309** 2180–4

[6] Chuang I L, Vandersypen L M K, Zhou X, Leung D W and Lloyd S 1998 Experimental realization of a quantum algorithm *Nature* **393** 143–6

[7] Cory D G *et al* 2000 NMR based quantum information processing: achievements and prospects *Fortschr. Phys.* **48** 875–907

[8] Cappellaro P, Jiang L, Hodges J S and Lukin M D 2009 Coherence and control of quantum registers based on electronic spin in a nuclear spin bath *Phys. Rev. Lett.* **102** 210502

[9] Vandersypen L M K, Steffen M, Breyta G, Yannoni C S, Sherwood M H and Chuang I L 2001 Experimental realization of Shor's quantum factoring algorithm using nuclear magnetic resonance *Nature* **414** 883–7

[10] Gulde S, Riebe M, Lancaster G P T, Becher C, Eschner J, Häffner H, Schmidt-Kaler F, Chuang I L and Blatt R 2003 Implementing the Deutsch–Jozsa algorithm on an ion-trap quantum computer *Nature* **421** 48

[11] Hodges J S, Cappellaro P, Havel T F, Martinez R and Cory D G 2007 Experimental implementation of a logical Bell state encoding *Phys. Rev.* A **75** 042320

[12] Chiaverini J *et al* 2005 Implementation of the semiclassical quantum Fourier transform in a scalable system *Science* **308** 997–1000

[13] DiCarlo L *et al* 2006 Demonstration of two-qubit algorithms with a superconducting quantum processor *Nature* **460** 240–4

[14] Schindler P, Barreiro J T, Monz T, Nebendahl V, Nigg D, Chwalla M, Hennrich M and Blatt R 2011 Experimental repetitive quantum error correction *Science* **332** 1059–61

[15] Campbell E T 2007 Distributed quantum-information processing with minimal local resources *Phys. Rev.* A **76** 040302

[16] Jiang L, Taylor J M, Sorensen A S and Lukin M D 2007 Distributed quantum computation based on small quantum registers *Phys. Rev.* A **76** 062323

[17] Bose S 2003 Quantum communication through an unmodulated spin chain *Phys. Rev. Lett.* **91** 207901

[18] Christandl M, Datta N, Ekert A and Landahl A J 2004 Perfect state transfer in quantum spin networks *Phys. Rev. Lett.* **92** 187902

[19] Christandl M, Datta N, Dorlas T C, Ekert A, Kay A and Landahl A J 2005 Perfect transfer of arbitrary states in quantum spin networks *Phys. Rev.* A **71** 032312

[20] Cappellaro P, Ramanathan C and Cory D G 2007 Simulations of information transport in spin chains *Phys. Rev. Lett.* **99** 250506

[21] Kay A 2007 Unifying quantum state transfer and state amplification *Phys. Rev. Lett.* **98** 010501

[22] Kay A 2010 Perfect, efficient, state transfer and its application as a constructive tool *Int. J. Quantum Inf.* **8** 641–76

[23] Weis C D *et al* 2008 Single atom doping for quantum device development in diamond and silicon *J. Vac. Sci. Technol.* B **26** 2596–600

[24] Toyli D M, Weis C D, Fuchs G D, Schenkel T and Awschalom D D 2010 Chip-scale nanofabrication of single spins and spin arrays in diamond *Nano Lett.* **10** 3168–72

[25] Naydenov B, Richter V, Beck J, Steiner M, Neumann P, Balasubramanian G, Achard J, Jelezko F, Wrachtrup J and Kalish R 2010 Enhanced generation of single optically active spins in diamond by ion implantation *Appl. Phys. Lett.* **96** 163108

[26] Spinicelli P *et al* 2011 Engineered arrays of nitrogen-vacancy color centers in diamond based on implantation of CN-molecules through nanoapertures *New J. Phys.* **13** 025014

IOP Institute of Physics · DEUTSCHE PHYSIKALISCHE GESELLSCHAFT

[27] Cappellaro P, Ramanathan C and Cory D G 2007 Dynamics and control of a quasi-one-dimensional spin system *Phys. Rev.* A **76** 032317

[28] Zhang W, Cappellaro P, Antler N, Pepper B, Cory D G, Dobrovitski V V, Ramanathan C and Viola L 2009 NMR multiple quantum coherences in quasi-one-dimensional spin systems: comparison with ideal spin-chain dynamics *Phys. Rev.* A **80** 052323

[29] Ramanathan C, Cappellaro P, Viola L and Cory D G 2011 Experimental characterization of coherent magnetization transport in a one-dimensional spin system *New J. Phys.* **13** 103015

[30] Rufeil-Fiori E, Sánchez C M, Oliva F Y, Pastawski H M and Levstein P R 2009 Effective one-body dynamics in multiple-quantum NMR experiments *Phys. Rev.* A **79** 032324

[31] Sur A, Jasnow D and Lowe I J 1975 Spin dynamics for the one-dimensional XY model at infinite temperature *Phys. Rev.* B **12** 3845–8

[32] Cho G and Yesinowski J P 1993 Multiple-quantum NMR dynamics in the quasi-one-dimensional distribution of protons in hydroxyapatite *Chem. Phys. Lett.* **205** 1–5

[33] Cho G and Yesinowski J P 1996 ^{1}H and ^{19}F multiple-quantum NMR dynamics in quasi-one-dimensional spin clusters in apatites *J. Chem. Phys.* **100** 15716–25

[34] Cappellaro P, Viola L and Ramanathan C 2011 Coherent-state transfer via highly mixed quantum spin chains *Phys. Rev.* A **83** 032304

[35] Munowitz M, Pines A and Mehring M 1987 Multiple-quantum dynamics in NMR: a directed walk through Liouville space *J. Chem. Phys.* **86** 3172–82

[36] Ramanathan C, Cho H, Cappellaro P, Boutis G S and Cory D G 2003 Encoding multiple quantum coherences in non-commuting bases *Chem. Phys. Lett.* **369** 311

[37] Fitzsimons J and Twamley J 2006 Globally controlled quantum wires for perfect qubit transport, mirroring, and computing *Phys. Rev. Lett.* **97** 090502

[38] DiFranco C, Paternostro M and Kim M S 2008 Perfect state transfer on a spin chain without state initialization *Phys. Rev. Lett.* **101** 230502

[39] Markiewicz M and Wiesniak M 2009 Perfect state transfer without state initialization and remote collaboration *Phys. Rev.* A **79** 054304

[40] Yao N Y, Jiang L, Gorshkov A V, Gong Z-X, Zhai A, Duan L-M and Lukin M D 2011 Robust quantum state transfer in random unpolarized spin chains *Phys. Rev. Lett.* **106** 040505

[41] Lieb E H and Mattis D C 1966 *Mathematical Physics in One Dimension; Exactly Soluble Models of Interacting Particles* (New York: Academic)

[42] Fel'dman E B and Lacelle S 1996 Multiple quantum NMR spin dynamics in one-dimensional quantum spin chains *Chem. Phys. Lett.* **253** 27–31

[43] Bodenhausen G, Kogler H and Ernst R R 1984 Selection of coherence-transfer pathways in NMR pulse experiments *J. Mag. Res.* **58** 370–88

[44] Keeler J 2010 *Understanding NMR Spectroscopy* (New York: Wiley)

[45] Davis A L, Estcourt G, Keeler J, Laue E D and Titman J J 1993 Improvement of Z filters and purging pulses by the use of zero-quantum dephasing in inhomogeneous $B1$ or $B0$ fields *J. Mag. Res.* **105** 167–83

[46] Oishi S and Kamiya T 1994 Flux growth of fluorapatite crystals *Nippon Kagaku Kaishi* **9** 800–4

[47] Yen Y-S and Pines A 1983 Multiple-quantum NMR in solids *J. Chem. Phys.* **78** 3579–82

[48] Sur A and Lowe I J 1975 NMR line-shape calculation for a linear dipolar chain *Phys. Rev.* B **12** 4597–603

[49] Engelsberg M, Lowe I J and Carolan J L 1973 Nuclear-magnetic-resonance line shape of a linear chain of spins *Phys. Rev.* B **7** 924

[50] Van der Lugt W and Caspers W J 1964 Nuclear magnetic resonance line shape of fluorine in apatite *Physica* **30** 1658–66

[51] Fel'dman E B and Lacelle S 1997 Multiple quantum nuclear magnetic resonance in one-dimensional quantum spin chains *J. Chem. Phys.* **107** 7067–84

[52] Doronin S, Maksimov I and Fel'dman E 2000 Multiple-quantum dynamics of one-dimensional nuclear spin systems in solids *J. Exp. Theor. Phys.* **91** 597–609

[53] Baum J, Munowitz M, Garroway A N and Pines A 1985 Multiple-quantum dynamics in solid state NMR *J. Chem. Phys.* **83** 2015–25

[54] Levy D H and Gleason K K 1992 Multiple quantum nuclear magnetic resonance as a probe for the dimensionality of hydrogen in polycrystalline powders and diamond films *J. Phys. Chem.* **96** 8125–31

[55] Cho H J, Ladd T D, Baugh J, Cory D G and Ramanathan C 2005 Multispin dynamics of the solid-state NMR free induction decay *Phys. Rev.* B **72** 054427

[56] Cho H J, Cappellaro P, Cory D G and Ramanathan C Decay of highly correlated spin states in a dipolar-coupled solid: NMR study of CaF_2 *Phys. Rev.* B **74** 224434